Optical and acoustic phonon temperature measurements using electron nanoprobe and electron energy loss spectroscopy

Jun Kikkawa [1,2,*] and Koji Kimoto [1]

[1] *Research Center for Advanced Measurement and Characterization, National Institute for Materials Science, 1-1 Namiki, Tsukuba 305-0044, Japan*

[2] *Japan Science and Technology Agency (JST), Precursory Research for Embryonic Science and Technology (PRESTO), 4-1-8 Honcho, Kawaguchi 332-0012, Japan*

(Received 4 March 2022; revised 11 November 2022; accepted 15 November 2022; published 29 November 2022)

Measuring temperature at a high spatial resolution is a fundamental technique for investigating local static and dynamic thermal properties in various materials and devices. Here, we report temperature measurement by electron energy loss spectroscopy using monochromated electron probes of 1–2 nm diameter and large scattering vectors of electrons and based on the principle of detailed balancing between the annihilation and creation of phonons. Temperatures defined by optical and acoustic phonons are evaluated separately. We demonstrate that the use of acoustic phonons is advantageous for low-temperature measurements with higher accuracy. The scheme is applied to evaluating local temperatures in a diamond nanowire during Joule heating. We also discuss the Joule heating mechanism and key factors for improving temperature measurement accuracy.

DOI: 10.1103/PhysRevB.106.195431

I. INTRODUCTION

Measuring temperature at a high spatial resolution is fundamental to understanding the local static and dynamic thermal properties in various materials and nanometer-scale devices in operation [1,2]. Extensive effort has been devoted to improving the spatial resolution and signals in measurements using optical techniques such as Raman spectroscopy [3–5]. The present tip-enhanced Raman scattering microscopy has a resolution of ∼10 nm [4]. However, the techniques involving scanning physical tips are only useful for surfaces. Another strategy for nanometer-resolution thermometry is the use of an electron probe based on transmission electron microscopy (TEM), which enables the analysis of thermal and structural properties at the same position. TEM-based thermometry has been carried out using schemes for Bragg scattering (BS) in electron diffraction (ED) [6], plasmons in electron energy loss spectroscopy (EELS) [7], and the intensity of electron-phonon scattering, i.e., thermal diffuse scattering (TDS) in ED [8]. However, these TEM-based techniques provide relative temperature differences and require conversion parameters, i.e., the thermal expansion coefficient for both BS and plasmon schemes and the Debye-Waller factor for TDS. It is unfavorable to apply BS and plasmon schemes to materials with small coefficients of thermal expansion such as diamond [9]. The TDS intensity depends on the specimen thickness and electron collection range.

Recently, high-energy-resolution (5–30 meV) EELS with TEM [10] has enabled us to measure temperature by probing the annihilation/creation ratio of phonons in electron-phonon scattering and based on the principle of detailed balancing [11–13]. One of the advantages of this method is that the absolute temperature is directly evaluated using a single spectrum without conversion parameters. The spatial resolution in scanning TEM (STEM)-EELS depends on $\mathbf{q}_\perp$, the component of the scattering vector of incident electrons $\mathbf{q}$ perpendicular to the incident direction [14,15]. Although the use of scattered electrons with $\mathbf{q}_\perp = 0$ and the energy transfer of millelectronvolt scale reduce the spatial resolution in EELS to ∼600–800 nm for 165 meV transfer with 80–200 keV electrons even when using a 1-nm-diameter probe (i.e., delocalization or nonlocality) [14,16], the use of scattered electrons with $\mathbf{q}_\perp \gg \mathbf{0}$ enables EELS with high spatial resolution equivalent to the probe size. Furthermore, STEM-EELS enables wave-vector-resolved phonon spectroscopy and spectrum imaging using acoustic phonons with specific wave vectors [15,17,18], which will be useful for phonon transport analysis. Temperatures for optical and acoustic phonons differ in nonequilibrium states of picosecond scale [19]. The time resolution is on the millisecond scale in practical STEM-EELS and in this paper, whereas it is enhanced to the femtosecond scale when using the pump-probe method [20]. Therefore, it is important to establish a technique to measure and analyze the temperatures using optical and acoustic phonons separately, although we measure temperatures in the steady states, i.e., equivalent optical and acoustic temperatures, in the framework of this paper.

In this paper, we evaluate the local temperature in diamond using either optical or acoustic phonons, using the large-$\mathbf{q}_\perp$ scheme in STEM-EELS and 1–2-nm-diameter electron probes. After examining the accuracy of temperature measurements by STEM-EELS using optical and acoustic phonons based on the results in Secs. III A and III B, respectively, we evaluate unknown temperatures in a diamond nanowire (DNW) during Joule heating in Sec. III C. The Joule heating mechanism and key factors for improving temperature measurement accuracy are discussed in Sec. IV.

*kikkawa.jun@nims.go.jp

II. METHOD

We used a single-crystal diamond obtained under high pressure and high temperature (Monodie MD111, Element Six, Ltd.). A thin diamond crystal (whose results are shown in Secs. III A and III B) and a DNW (whose results are shown in Sec. III C) were prepared for EELS using a focused ion beam (FIB; NB5000, Hitachi High-Tech, Co.). The thin diamond crystal was fixed on a holey ceramic membrane in an electrical chip [Thermal E-chip, Protochips, Inc.; Fig. 1(a)] using a thermally conductive epoxy resin. The DNW was fabricated on an electrical chip (FIB-optimized E-chip, Protochips, Inc.). The chips were attached to an electric-biasing TEM holder (Aduro300N, Protochips, Inc.). The length, width, thickness, and crystallographic orientation of the DNW were 10.4 μm, 400 nm, 340 nm, and [11$\bar{1}$], respectively. A source measure unit (Model 2636B, Keithley Instruments, Inc.) was used to apply electric bias for the Joule heating of either the membrane (Secs. III A and III B) or the DNW (Sec. III C). We refer to the nominal temperature of the membrane T_n calibrated with electrical bias by the manufacturer (Protochips, Inc.) with a 5% error [21]. A monochromated electron microscope (Themis Z, Thermo Fisher Scientific, Inc.) equipped with a spectrometer (Quantum 970, Gatan Inc.) was used for EELS. The electron incident direction to the thin diamond crystal and DNW was [1$\bar{1}$0].

For EELS whose results are shown in Sec. III A, we used a 200 keV electron probe with a diameter of $\sim$1 nm, a convergence semiangle α of 2.8 mrad ($= 7.0\,\mathrm{nm}^{-1}$), and beam currents of 5–7 pA ($= 3 \times 10^7$ to 4×10^7 electrons s^{-1}). We used a collection semiangle β [i.e., radius of the wave-vector-selected circle in Fig. 1(b)] of 3.1 mrad ($= 7.7\,\mathrm{nm}^{-1}$), the spectrometer with an energy dispersion of 5.29 meV/ch, and a complementary metal-oxide-semiconductor-based direct-electron-detection camera (K2 IS, Gatan Inc.). The full width at half maximum (FWHM) of the zero-loss peak (ZLP) was 21.2 meV. Electrons scattered at/around the 222 diffraction disk (i.e., 2**g** when defining the 111 reciprocal point as **g**; forbidden reflection) within the radius β and the Γ point at the circle center were collected for EELS [Fig. 1(b)] and the phonon dispersion [Fig. 1(c)] [15,22]. The exposure time and the total number of frames for phonon measurements were set to 49.2 ms/frame and 2500, respectively. A single spectrum at T_n was obtained after ZLP alignment for all 2500 spectra, and then their sum was obtained. The specimen thickness of the measurement area (Fig. 2) was $\sim$150 nm. After the initial EELS at $T_n = 303$ K, it was subsequently conducted at temperatures increased from 373 to 1473 K at 50 K intervals with heating for $\sim$10 min at each temperature before EELS. Because the heating area of the membrane was 10^3–$10^4\,\mu\mathrm{m}^2$, which was larger than the diamond specimen area ($\sim 10^2\,\mu\mathrm{m}^2$), and the epoxy resin and diamond have high thermal conductivities, the diamond temperature was expected to be T_n at an equilibrium state.

For EELS whose results are shown in Sec. III B, we used an 80 keV electron probe with a diameter of $\sim$2 nm, α of 1.5 mrad ($= 2.3\,\mathrm{nm}^{-1}$), a beam current of $\sim$ 3.4 pA ($= 2.1 \times 10^7$ electrons s^{-1}), and β of 1.8 mrad ($= 2.7\,\mathrm{nm}^{-1}$); the spectrometer with an energy dispersion of 3.78 meV/ch; and a charge-coupled device (CCD) camera with a high-sensitivity scintillator (994US1000XP U+, Gatan Inc.). The conversion efficiency of the CCD was 27.6 counts per electron collision for 80 keV. The FWHM of the ZLP was 18.2 meV. A 9.5-μm-diameter condenser aperture was used to set α. Electrons scattered at/around 1.5**g** (L point) within the radius

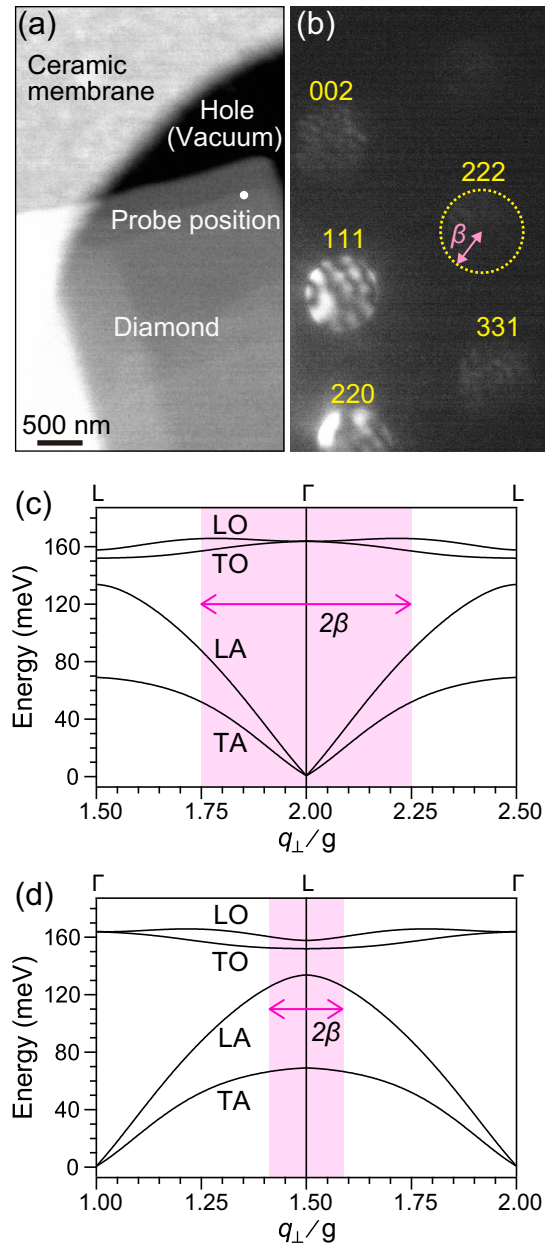

FIG. 1. (a) Annular dark-field (ADF)-scanning transmission electron microscopy (STEM) image of the diamond crystal partially supported on a ceramic membrane. The diamond temperature is increased by the Joule heating of the membrane. (b) Diffraction disks from the diamond crystal obtained using an $\sim$1-nm-diameter electron probe and the [1$\bar{1}$0] electron incident direction as described in Sec. III A. The center of the wave-vector-selected aperture denoted by the dotted circle was placed at the 222 reciprocal lattice point (Γ point) for electron energy loss spectroscopy (EELS). The radius of the aperture β is $7.7\,\mathrm{nm}^{-1}$. Phonon dispersion curve of diamond (solid line) [22] and the collection range (i.e., 2β) for EELS in (c) Sec. III A and (d) Sec. III B: $\beta = 2.7\,\mathrm{nm}^{-1}$ for EELS in Sec. III.

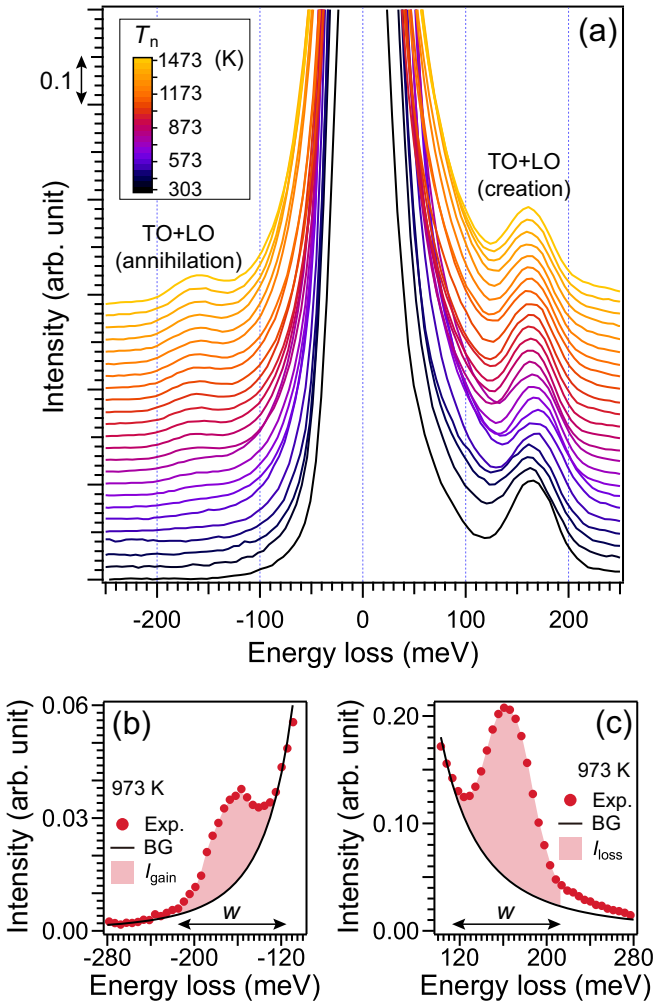

FIG. 2. (a) Changes in electron energy loss spectroscopy (EELS) spectra acquired from diamond crystal with T_n between 303 and 1473 K. Replots (solid circles) of (b) gain and (c) loss sides of EELS at 973 K in (a) with background curves (solid lines). The shaded areas in (b) and (c) denote I_{gain} and I_{loss} at 973 K, respectively. The intensity of each spectrum in (a) is normalized by I_{loss} of 1.7–8.5 $\times$ 10^4 electron counts.

β were collected for EELS [Fig. 1(d)]. The exposure time and total frame number for phonon measurements were set to 40 ms/frame and 10 000, respectively. A single spectrum at T_n was obtained after ZLP alignment for all 10 000 spectra, and then their sum was obtained. The specimen thickness of the measurement area was ∼130 nm. We used a ZLP acquired in vacuum (i.e., >1 μm away from the edge of objects) as the kernel for Richardson-Lucy deconvolution (RLD) [23,24]. The number of iterations of the RLD was 7–9.

For STEM-EELS whose results are shown in Sec. III C, a constant electric bias of 20 V was applied to the Joule heating of the DNW, with electric currents of 160–170 μA in the steady state. We used an 80 keV electron probe with a diameter of ∼2 nm, α of 1.5 mrad (= 2.3 nm^{-1}), a beam current of ∼ 5 pA (= 3 $\times$ 10^7 electrons s^{-1}), a scanning step of 5.07 nm, and β of 5.8 mrad (= 8.7 nm^{-1}); the spectrometer with an energy dispersion of 3.78 meV/ch; and the CCD camera. The β larger than that in Sec. III B was used with the aim of increasing the signal-to-noise ratio in EELS. Electrons scattered at/around 1.5**g** (L point) within the radius β were collected for EELS. The exposure time at each probe position was set to 40 ms. For RLD processing, we used a ZLP acquired in vacuum as the kernel and the number of iterations of 9–15. The C K-edge spectra of the DNW were acquired using an 80 keV electron probe with α of 35 mrad (= 53 nm^{-1}) and β of 18 mrad (= 27 nm^{-1}). Diffraction patterns were obtained by spatially resolved diffractometry [25] and subsequent data integration in the area of interest.

III. RESULTS

A. Temperature measurement using optical phonon

A thin single-crystal diamond fixed on a holey ceramic membrane, as shown in Fig. 1(a), was heated by Joule heating of the membrane. Using an ∼1-nm-diameter probe located on the specimen [Fig. 1(a)] and collecting electrons scattered at/around 2**g** with β = 7.7 nm^{-1} [Figs. 1(b) and 1(c)], we acquired a series of EELS spectra at T_n between 303 and 1473 K, as shown in Fig. 2(a). On the positive (i.e., energy loss) side, the peak ∼165 meV indicates the creation of optical phonons as a result of energy transfer from incident electrons to the lattice system, where the transverse optical (TO) and longitudinal optical (LO) modes are degenerated at the Γ point [15,22]. On the negative (i.e., energy gain) side, the peak ∼−165 meV indicates the annihilation of the degenerated optical phonons as a result of energy transfer from the vibrating lattice system to the incident electrons. As shown in Figs. 2(b) and 2(c), we respectively define $I_{loss,\ TO+LO}$ and $I_{gain,\ TO+LO}$ as the total electron counts for phonons within the integral width w of 100.5 meV (= 19 channels) on the loss and gain sides (i.e., shaded areas) after background subtraction by power law fitting [26]. Each spectrum intensity in Fig. 2(a) is normalized by $I_{loss,\ TO+LO}$. The result in Fig. 2(a) indicates that $I_{gain,\ TO+LO}$ increases relative to $I_{loss,\ TO+LO}$ with increasing T_n. A plot of $I_{gain,\ TO+LO}/I_{loss,\ TO+LO}$ as a function of T_n is shown in Fig. 3(a) (right vertical axis). The lateral and vertical error bars in Fig. 3(a) originate from the 5% error in T_n [21] and the fitting parameters for background subtractions, respectively. In EELS throughout this paper, an incident electron arrives every 2 $\times$ 10^{-7} to 4 $\times$ 10^{-7} s on average, which is greater than the lifetime of optical phonons for diamond (i.e., 2.9 $\times$ 10^{-12} s at 300 K [27] and less at higher temperatures) [28–30]. The phonon energy is ∼ 10^{-6} of incident electron energy, i.e., 80–200 keV. Therefore, we can consider the present EELS measurement as the interaction between a time-dependent weak external probe (i.e., electron nanoprobe) and the many-particle (i.e., phonons) system in a thermal equilibrium state, where the Born approximation is valid [13]. The present measurement satisfies the principle of detailed balancing between phonon creation and annihilation, expressed as (see Appendix) [13]

$$I_{gain}/I_{loss} = \exp\left(-\frac{E_{ph}}{k_B T_{ph}}\right), \quad (1)$$

where E_{ph}, k_B, and T_{ph} are the phonon energy, the Boltzmann constant, and the temperature at the electron probe position, respectively: we refer to T_{ph} as the *phonon temperature* to dis-

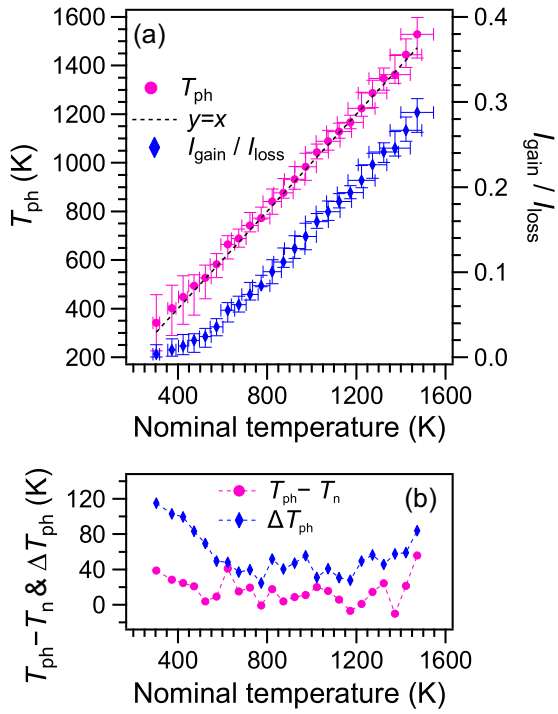

FIG. 3. (a) Plots of I_{gain}/I_{loss} (right axis) and T_{ph} $(= -E_{ph}/[k_B \ln(I_{gain}/I_{loss})])$ (left axis) in Fig. 2 as functions of the nominal temperature T_n. The dotted line denotes $y = x$ as a guide. Lateral and vertical error bars originate from the 5% error in T_n and the fitting parameters for the background subtraction in Figs. 2(b) and 2(c), respectively. (b) Plots of the temperature difference $T_{ph} - T_n$ and the average error ΔT_{ph} $[= (T_{ph,max} - T_{ph,min})/2]$ as functions of T_n.

tinguish it from the nominal temperature of the membrane T_n. Equation (1) states that the probabilities of phonon creation and annihilation (i.e., I_{loss} and I_{gain}, respectively) in a thermal equilibrium state are not independent of each other and are related to the Boltzmann factor. Using Eq. (1) and the measured E_{ph} as the center position of optical phonons at T_n, we evaluated T_{ph} $\{= -E_{ph}/[k_B \ln(I_{gain,\ TO+LO}/I_{loss,\ TO+LO})]\}$ and plotted it in Fig. 3(a) (left vertical axis), where the dotted line denotes $y = x$ as a guide. Here, T_{ph} for diamond at the probe position is approximately equivalent to T_n. Thus, the result demonstrates that the local temperature in nonpolar crystals (i.e., diamond here) can be measured using an ∼1-nm-diameter electron probe and a large scattering vector $\mathbf{q}_\perp$ ($\gg 0$) and based on the principle of detailed balancing. The use of impact scattering with a large $\mathbf{q}_\perp$ in this paper results in a spatial resolution superior to that obtained when using dipole scattering ($\mathbf{q}_\perp = 0$), which is demonstrated in Sec. III C.

Figure 3(b) shows plots of the difference between phonon and nominal temperatures ($T_{ph} - T_n$) and the average error in T_{ph} (ΔT_{ph}) defined as $\Delta T_{ph} = (T_{ph,max} - T_{ph,min})/2$, as functions of T_n, where $T_{ph,max}$ and $T_{ph,min}$ are the maximum and minimum T_{ph} with respect to the parameters of power law fitting, respectively. The accuracy of T_{ph} deteriorates $\sim< 500$ K and > 1400 K. The deterioration at higher temperatures is due to the increase in the number of thermally excited acoustic phonons, which makes the power law fitting for the ZLP intensity subtraction difficult on the gain side. The deterioration < 500 K is due to the decrease in signal-to-noise ratio for $I_{gain,\ TO+LO}$. Because the number of thermally excited optical phonons decreases at lower temperatures, the probability of phonon annihilation, i.e., $I_{gain,\ TO+LO}$, decreases as shown in Fig. 2(a). One of the strategies to improve the accuracy of $T_{ph} < 500$ K is to use lower-energy phonons such as transverse acoustic (TA) and longitudinal acoustic (LA) phonons with adequate wave vectors, as illustrated in dispersion curves in Fig. 1(d). The probability of finding thermally excited phonons in the TA mode is expected to be higher than that in optical modes (i.e., TO + LO) at a given low temperature T_n (see Sec. III B) [15,22]. We focus on the TA phonons in Sec. III B.

B. Temperature measurement using acoustic phonons

To investigate the possibility of T_{ph} evaluation using TA phonons, we obtained EELS spectra using $\mathbf{q}_\perp = 1.5\mathbf{g}$ and $\beta = 2.7\ \mathrm{nm}^{-1}$ [Fig. 1(d)] at T_n between 323 and 523 K. Figure 4(a) shows logarithmic plots of the raw spectrum (dotted line) at 323 K and its deconvolved spectrum (solid line) by RLD (see Sec. II). The intensities of phonon creation in the TA, LA, and TO + LO modes are located with the peak centers at 68.9, 124.5, and 151.8 meV, respectively. On the other hand, the intensity of phonon annihilation in the TA mode is clearly visible and that in the LA mode is faintly visible in Fig. 4(a). The intensity of phonon annihilation for the TO + LO mode is not visible in Fig. 4(a): a convex (2 ch width, $0.39\ \mathrm{s}^{-1}$ maximum) at −154.5 meV in the raw spectrum is probably due to noise. The energy dependence of signal strength for phonon annihilation is qualitatively expected from the finding probability W_m [Eq. (A3)]. The finding probability W_m for LA phonons (W_{LA} with 124.5 meV) and that for TO + LO phonons (W_{TO+LO} with 151.8 meV) are, respectively, 0.153 and 0.046 times that for TA phonons (W_{TA} with 68.9 meV), clearly indicating the advantage of using lower-energy acoustic phonons (see Appendix).

For evaluating the intensities of TA modes, i.e., $I_{loss,\ TA}$ and $I_{gain,\ TA}$, power law fitting was not useful for both the raw and RLD-processed spectra [Fig. 4(a)] owing to the presence of intensities of ZLP and LA phonons, which is different from the case of $\mathbf{q}_\perp = 0$ in Fig. 2(a). Thus, we applied multiple Gaussian fittings to the spectra after being processed by RLD. Figure 4(b) shows a series of the deconvolved spectra at T_n between 323 and 523 K, where each spectrum intensity in Fig. 4(b) is normalized by $I_{loss,\ TA}$ with an integral width of 64.3 meV. Figure 4(c) shows the Gaussian fits for the spectrum at 323 K. The following procedure was used for fitting: (i) fitting for the ZLP using two profiles; (ii) fitting for TA (loss) and fixing its Gaussian center; (iii) fitting for LA (loss) and TO + LO (loss) and fixing their Gaussian center; (iv) fitting for TA (gain), fixing its Gaussian center with the negative value of the Gaussian center for TA (loss) and adjusting the FWHM with an increase by 1–6 ch (i.e., 3.78–22.7 meV) from the value of the FWHM for TA (loss); (v) fitting for LA (gain) as in (iv). Then $I_{loss,\ TA}$ and $I_{gain,\ TA}$ were calculated as integral intensities within the width w, as indicated in Fig. 4(c). Using $I_{loss,\ TA}$, $I_{gain,\ TA}$, and Eq. (1), we evaluated T_{ph} $\{= -E_{ph}/[k_B \ln(I_{gain,\ TA}/I_{loss,\ TA})]\}$ for each w, i.e., $w = 9$–17 ch $(= 34.1$–64.3 meV) and obtained

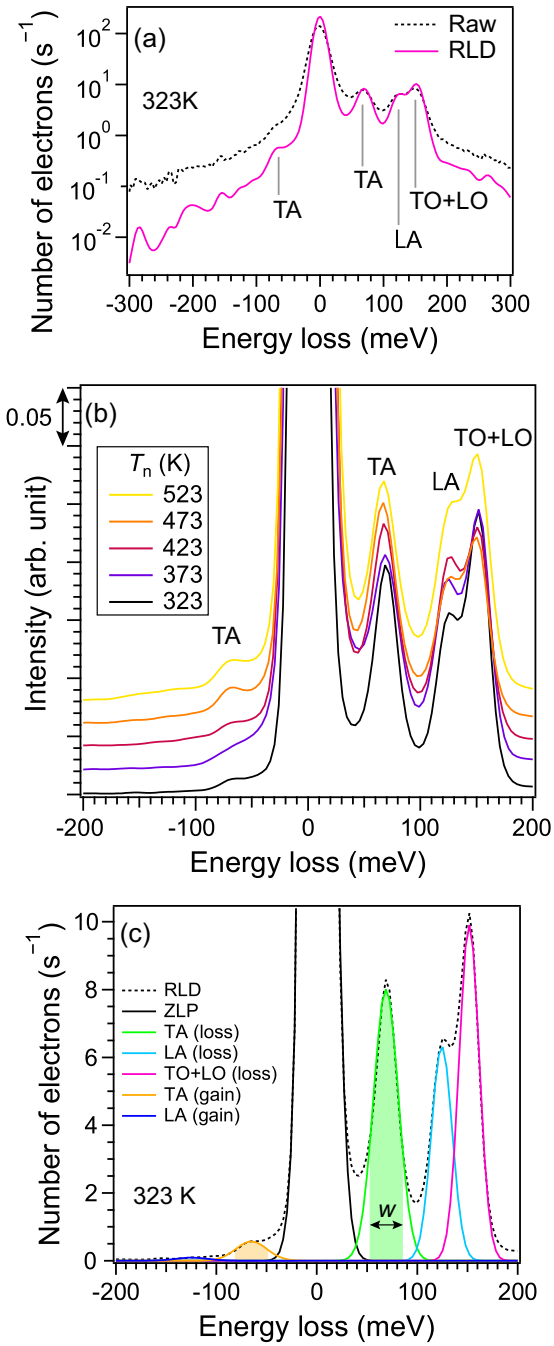

FIG. 4. (a) Logarithmic plots of the raw (dotted line) and Richardson-Lucy deconvolution (RLD)-processed (solid line) electron energy loss spectroscopy (EELS) spectra with $\mathbf{q}_\perp = 1.5\mathbf{g}$ and $\beta = 2.7\,\mathrm{nm}^{-1}$ [Fig. 1(d)] at $T_\mathrm{n} = 323\,\mathrm{K}$ and (b) the deconvolved spectra at T_n between 323 and 523 K. (c) Multiple Gaussian fits for the deconvolved spectrum at $T_\mathrm{n} = 323\,\mathrm{K}$. $I_{\mathrm{loss,\,TA}}$ is defined as the integrated intensity of the Gaussian profile for transverse acoustic (TA) within the constant widths w of 34.05–64.3 meV (9–17 channels). The intensity of each spectrum in (b) is normalized by $I_{\mathrm{loss,\,TA}}$ with $w = 64.3\,\mathrm{meV}$, 2.5–3.2 $\times\,10^4$ electron counts.

$T_\mathrm{ph} = 342 \pm 10\,\mathrm{K}$ at $T_\mathrm{n} = 323\,\mathrm{K}$. Figure 5(a) shows a plot of T_ph for the TA mode at T_n from 323 to 523 K, where the dotted line denotes $y = x$ as a guide. Lateral and vertical error bars originate from the 5% error in T_n and the choice of w

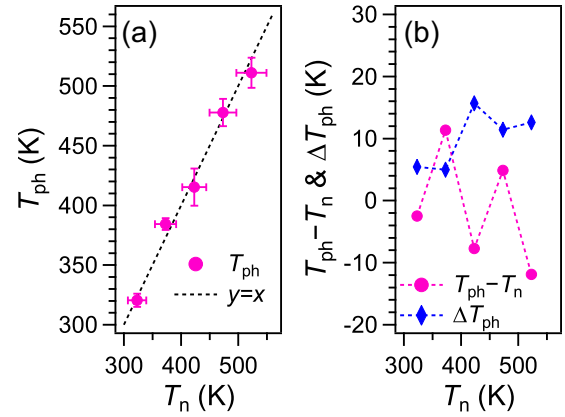

FIG. 5. (a) Plots of T_ph $(= -E_\mathrm{ph}/[k_\mathrm{B}\ln(I_{\mathrm{gain,TA}}/I_{\mathrm{loss,TA}})])$ as a function of T_n, derived from Fig. 4(b). The dotted line denotes $y = x$ as a guide. Lateral and vertical error bars originate from the 5% error in T_n and the choice of w for count integration in Fig. 4(c). (b) Plots of the temperature difference $T_\mathrm{ph} - T_\mathrm{n}$ and the deviation ΔT_ph as functions of T_n.

for count integration in Fig. 4(c). The T_ph evaluated using TA phonons is approximately equivalent to T_n. Figure 5(b) shows plots of the difference between phonon and nominal temperatures ($T_\mathrm{ph} - T_\mathrm{n}$) and the absolute value of the error in T_ph (ΔT_ph) as functions of T_n. It is notable that T_ph is evaluated more accurately when using acoustic phonons [Fig. 5(b)] than when using optical phonons in Fig. 3(b). Thus, the result demonstrates the advantages of using acoustic phonons at low temperatures.

C. Application to DNW for Joule heating

Here, the techniques whose results are shown in Sec. III B are applied to evaluating unknown temperatures during Joule heating. Figure 6(a) shows an annular dark-field (ADF)-STEM image of the DNW of 400 nm width and 350 nm thickness. The DNW has a single crystal core (i.e., $20 \lesssim y \lesssim 330\,\mathrm{nm}$) and amorphous carbon (a-C) layers on its both sides (i.e., $0 \leqslant y \lesssim 20\,\mathrm{nm}$ and $330 \lesssim y \leqslant 400\,\mathrm{nm}$) along the x direction, as shown in an ADF-STEM image [Fig. 6(b)] acquired with the center of the ADF detector at $1.5\mathbf{g}$. The a-C properties are described in detail in Sec. IV. The a-C layers were formed owing to 30 kV Ga^+ ion bombardments, whereas the a-C layers on top and bottom surfaces of the DNW were reduced by 5 kV Ga^+ ion milling. By applying a voltage of 20 V to the DNW, STEM-EELS was performed in the entire area of Fig. 6(b) with a scanning step of 5.07 nm. Figure 6(c) shows an EELS map along the y direction acquired from the rectangle area ($-50.7 < x \leqslant 45.6\,\mathrm{nm}$) in Fig. 6(b), where 20 spectra along the x direction were averaged. The created TO + LO phonons are clearly visible and easily counted at 155 meV in the diamond area, whereas the annihilated TO + LO phonons are faintly visible. The intensities of ZLP and its tails in the a-C area are higher than those in the diamond area, reflecting an elastic scattering distribution. Figure 6(d) shows EELS profiles for diamond and a-C areas averaged in the ranges of $60.8 \leqslant y \leqslant 324.4\,\mathrm{nm}$ and $349.8 \leqslant y \leqslant 395.4\,\mathrm{nm}$, respectively, in Fig. 6(c) and processed by RLD (see Sec. II). The spectrum for diamond (solid line) in Fig. 6(d) indicates

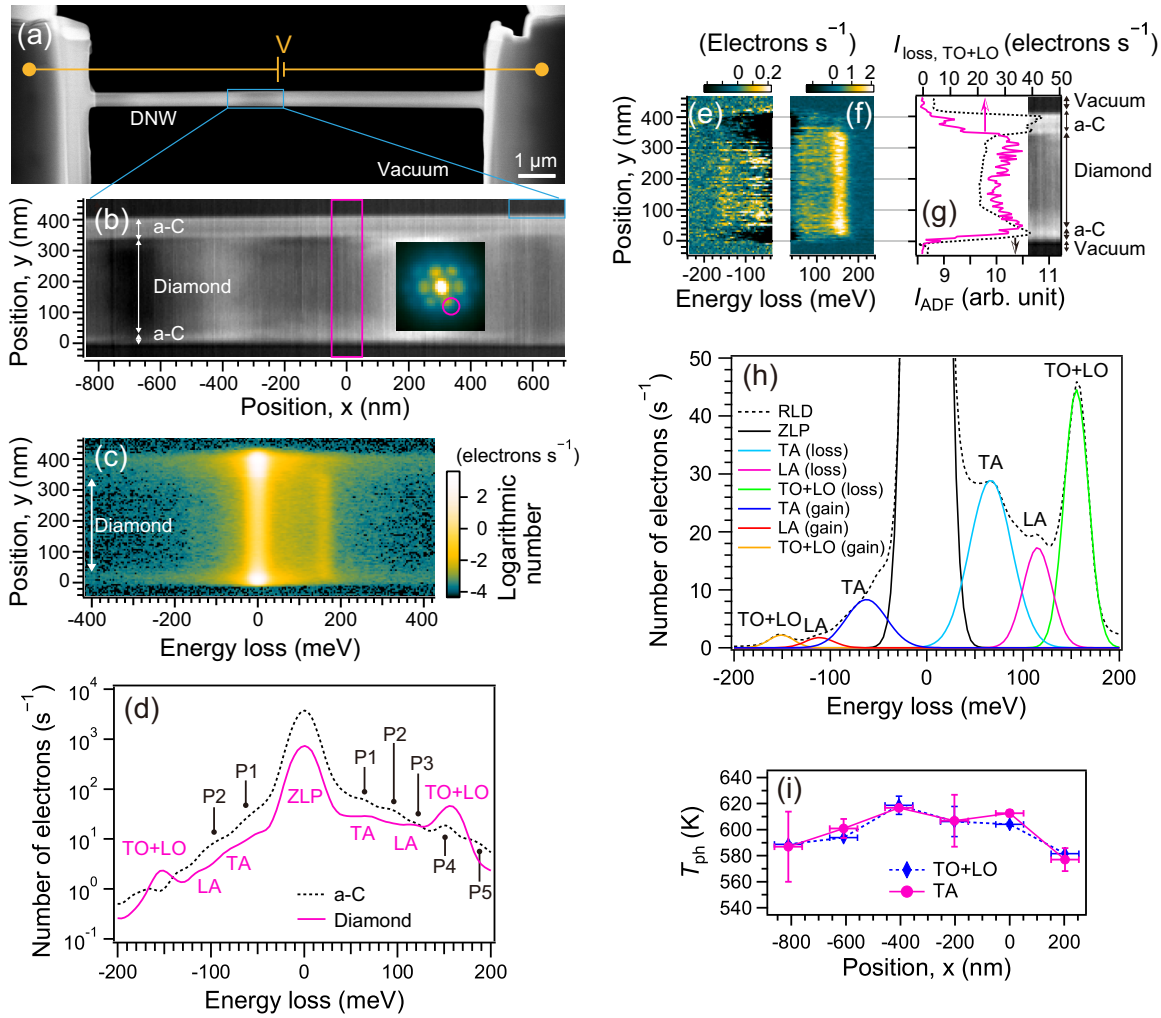

FIG. 6. (a) Annular dark-field (ADF)-scanning transmission electron microscopy (STEM) image of the diamond nanowire (DNW) in vacuum. A constant electric bias of 20 V was applied between bulk parts at both ends of the DNW. (b) Enlarged off-axis STEM image of the rectangle area in (a), obtained by setting the ADF detector center at 1.5**g**. (c) Averaged electron energy loss spectroscopy (EELS) map in the x direction acquired from the rectangular area in (b). The solid circle in the inset diffraction pattern for the diamond area indicates the collection range for EELS. (d) EELS profiles averaged in the diamond (solid line) and a-C (dotted line) areas in (c). P1–P5 indicate phonon modes for a-C. Parts of EELS map in (c) for (e) gain and (f) loss areas after subtracting tails of the zero-loss peak (ZLP). (g) Profiles in the y direction for the integrated $I_{loss,\ TO+LO}$ in (f) (solid line) and ADF intensity in the inset image cut from rectangular area in (b). (h) Multiple Gaussian fits for the Richardson-Lucy deconvolution (RLD)-processed profile for diamond in (d). (i) Plots of T_{ph} for transverse acoustic (TA; solid line) and transverse optical (TO) + longitudinal optical (LO; dotted line) along the x direction in (b).

the presence of created TA and LA phonons and annihilated TA, LA, and TO + LO phonons in Fig. 6(c). Since the TO + LO phonon intensity in Fig. 6(d) is relatively higher than that in Fig. 4(a), we can infer that the temperature is $>$ 500 K. The spectrum for a-C (dotted line) in Fig. 6(d) also reveals a characteristic profile and the phonon-derived maxima are indicated by P1–P5: other lower maxima on the gain side are derived from noises. The P1–P5 peaks are located at ∼65, 95, 120, 152, and 180 meV. The P1–P3 peaks are ascribed to vibrational modes of sp^3 bonds in a-C, whereas the P4 and P5 peaks are ascribed to vibrational modes of sp^2 bonds in a-C [31]. The P1 and P2 peaks are visible on the gain side, implying that a-C areas are also heated. Figures 6(e) and 6(f), respectively, show parts of gain and loss areas of EELS maps [Fig. 6(c)] after subtracting tails of the ZLP on the energy-loss and energy-gain sides with power law fits. The counts of created TA and LA phonons (∼65 and 115 meV, respectively) in Fig. 6(f) and annihilated TA, LA, TO + LO phonons (∼−65, −115, and −155 meV, respectively) in Fig. 6(e) are discrete along the y direction. This is simply because the average count of phonons created and annihilated during the exposure time at each spectrum is $<$1: continuous count distributions can be obtained with longer exposure time (i.e., taking the time average). Figure 6(g) shows profiles of integrated counts of TO + LO phonons (solid line), i.e., $I_{TO+LO,loss}$ in Fig. 6(e) and ADF intensity (dotted line) in the inset along the y direction. The intensity of $I_{TO+LO,loss}$ varies steeply at the diamond/a-C interfaces like the ADF intensity, implying that spatially resolved phonon spectroscopy is achieved using large **q**: the phonon spectroscopy resolution in Fig. 6 is $<$ 10 nm (= 2 pixel). Figure 6(h) shows multiple Gaussian fits for the RLD-processed profile in Fig. 6(d). Using the fit

profiles for TA and also TO + LO phonons, we evaluated phonon temperatures (T_{ph}) averaged in the rectangle centered at $x = 0$ in Fig. 6(b), which is analogous to Fig. 4(c). Here, T_{ph} values for TA and TO + LO phonons were evaluated as 613 ± 5 and 603 ± 3 K, respectively. Also, T_{ph} values at different center positions (x) of the rectangle were also evaluated and are plotted in Fig. 6(i). The T_{ph} values in the TA and TO + LO modes are similar, reflecting that the T_{ph} distribution is in the steady state during measurements: a large difference in T_{ph} between the TA and TO + LO modes can occur in the picosecond-scale nonsteady state [19]. Figure 6(i) shows the T_{ph} profile in the range of $-800 \leqslant x \leqslant 200$ in Fig. 6(b), with a maximum of ~620 K at around $x = -400$ nm. In Fig. 6, the spatial resolution is reduced by binning along both the x and y directions to obtain T_{ph} with high accuracy because the phonon count at each pixel (5.07×5.07 nm) was low owing to the short exposure time (40 ms). By increasing the total exposure time (40–50 s) at each pixel, we may obtain T_{ph} maps maintaining the spatial resolution at 5.07 nm in principle.

IV. DISCUSSION

A. Joule heating mechanism

Figure 7(a) shows the applied constant voltage and electrical current across the DNW as functions of time. The current is constant with time after applying voltages up to 8.0 V, whereas the current decreases with time until it reaches a steady state after applying voltages > 9.0 V. Decreases in the current density **J** means increases in the electrical resistivity ρ and decreases in the electron mobility μ in the DNW, i.e., $\mathbf{J} \propto \rho^{-1}$ and $\mathbf{J} \propto \mu$, respectively. The decrease in μ occurs because of the increase in the number of excited phonons (i.e., increase in temperature) and electron-phonon scattering: the mobility for acoustic phonon scattering is proportional to $T^{-3/2}$ [32]. Here, ρ can be estimated using $R = \rho \frac{L}{A}$, where R is the electrical resistance and L and A are, respectively, the length and cross-sectional area of the conductor. This DNW has a-C layers on both sides of the core diamond part, as shown in the C K edge by EELS and diffraction patterns for the a-C and diamond areas in Fig. 7(b). Because the ρ values are 1–10^{-5} and 10^{12}–10^{18} Ωm at ~ 300 K for a-C and diamond (type Ib, HPHT method), respectively [33,34], the a-C parts are expected to be conductive paths. Using $L = 1.04 \times 10^{-5}$ m and $A = 2.38 \times 10^{-14}$ m^2 for a-C parts as the conductive paths and $R = 0.13$ MΩ when applying 1 V, ρ of a-C is calculated to be 3.0×10^{-4} Ωm, which agrees with a previous report [33]. Assuming diamond as a conductor, ρ is calculated to be 1.4×10^{-3} Ωm, which is not acceptable [34]. Thus, electron flow and Joule heating occurred in the a-C areas of the sides of DNW along the x direction when applying voltages, as illustrated in Fig. 7(c). On the other hand, the thermal conductivity κ values of a-C and diamond (type Ib, HPHT method) are reported to be 0.1–2 and 1000–2000 W m^{-1} K^{-1}, respectively [35,36]. This implies that heat dissipation by phonon transport occurs through the core diamond along the x direction, after phonons in a-C areas are transported to the core diamond areas, as illustrated in Fig. 7(c). The temperature distribution reaches the steady state with time. In Fig. 6(i), the temperature gradient is roughly ±0.1 K nm^{-1} on both sides at around $x = -400$ nm, which is the temperature

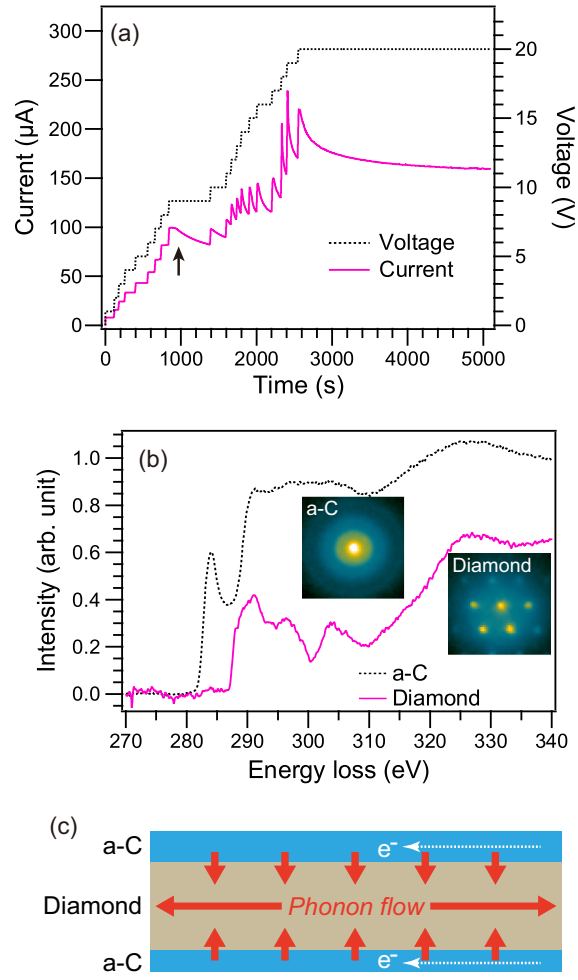

FIG. 7. (a) Profiles of constant voltage (dotted line) and electrical current (solid line) across the diamond nanowire (DNW) in Fig. 6(a) as functions of time. (b) C K edges and insets of diffraction patterns acquired in the a-C and diamond areas. (c) Illustration of the Joule heating mechanism. The dotted and solid arrows indicate the directions of flows of electrons and phonons, respectively.

maximum point. From Fourier's law with the magnitude of the gradient 0.1 K nm^{-1} and κ of ~ 10^{-6} W nm^{-1} K^{-1} [36], the heat flux in the core diamond area along x is estimated to be ~ 10^{-7} W nm^{-2}.

B. For improving the accuracy of temperature measurement

To improve the T_{ph} accuracy to probe a specific phonon mode by STEM-EELS, a spectrum should show (i) clearly separated phonon peaks and (ii) a sufficiently large signal-to-noise ratio especially for gain sides. To achieve (i), the wave vector resolution must be sufficiently high in addition to the energy resolution. In the case of optical phonons, poor wave vector resolution causes improper fitting for the ZLP intensity subtraction, especially at high temperatures with an increased number of thermally excited acoustic phonons, resulting in a low poor T_{ph} accuracy [Fig. 3(b)]. In the case of acoustic phonons, measurements at reciprocal points with high symmetry [such as L points in Fig. 1(d)] are effective because the symmetry of the phonon dispersion halves the actual wave number resolution. To achieve (ii), it is effective to use

phonons with lower energies, i.e., acoustic phonons, because the number of thermally excited phonon is larger, as described in Sec. III B. Therefore, it is effective to conduct STEM-EELS with higher wave vector resolution at a high symmetric reciprocal point (e.g., the L point) to obtain a higher $T_{\rm ph}$ accuracy. In this case, optical and acoustic phonons can be simultaneously measured separately, and $T_{\rm ph}$ with acoustic phonons is more accurate in low-temperature regions. As increasing wave vector resolution reduces the number of collected inelastic electrons per time for EELS, a longer exposure time and thus the stability of the STEM-EELS system (i.e., the time-invariant ZLP position) are required. It is practically important that the wave vector, energy, and spatial resolutions are increased with an appropriate balance for the measurement system.

V. CONCLUSIONS

We measured local optical and acoustic phonon temperatures of diamond in the steady state using an electron probe with a diameter of 1–2 nm, EELS with a large scattering vector, and the principle of detailed balancing between the annihilation and creation of the phonons. It was demonstrated that the accuracy of temperature measurement using acoustic phonons is superior at lower temperatures. We applied the scheme to the evaluation of local temperatures in the DNW during Joule heating and briefly discussed the heating mechanism. In this paper, we pave the way for ∼1-nm-resolution temperature mapping in various materials and devices by probing acoustic phonons with higher-wave-vector resolution, high-energy resolution, and instrument stability.

ACKNOWLEDGMENTS

This paper was supported by JST PRESTO Grant No. JPMJPR18I4 and JSPS KAKENHI Grants No. 22H01959 and No. 20H02624. Specimens were prepared using the FIB with the support of the NIMS Electron Microscopy Analysis Station. J.K. thanks Y. Nakayama and S. Shimomura (NIMS) for assistance in specimen preparation.

APPENDIX: THEORETICAL ASPECT

EELS intensity I is proportional to the differential cross-section for inelastic scattering $\frac{d^2\sigma}{d\Omega dE}$ [26]. Using the wave numbers of incident and scattered electrons (k_0 and k), the scattering vector $\mathbf{q}$, the energy transfer from incident electron to the system (i.e., energy loss of incident electron E) the initial and final states of the system $|m\rangle$ and $|n\rangle$ with energies E_m and E_n, and the probability for finding the initial state (W_m) [13], we can write the differential cross-section at finite temperature within the Born approximation as

$$\begin{aligned} I(\mathbf{q},\ E) &\propto \frac{d^2\sigma}{d\Omega dE} \\ &= \frac{m_0^2 e^2}{4\pi^2\epsilon_0^2\hbar^4 q^4}\frac{k}{k_0}\frac{1}{N}\sum_{m,n} W_m |\langle n|\int d\mathbf{r}\rho(\mathbf{r}) \\ &\quad \times \exp(-2\pi i\mathbf{q}\cdot\mathbf{r})|m\rangle|^2\delta(E-E_n+E_m) \\ &= \frac{m_0^2 e^2}{4\pi^2\epsilon_0^2\hbar^4 q^4}\frac{k}{k_0}\frac{1}{N}S(\mathbf{q},\ E), \end{aligned} \tag{A1}$$

where $S(\mathbf{q},\ E)$ is the dynamic form factor:

$$\begin{aligned} S(\mathbf{q},\ E) = \sum_{m,n} W_m |\langle n|\int d\mathbf{r}\rho(\mathbf{r}) \\ \times \exp(-2\pi i\mathbf{q}\cdot\mathbf{r})|m\rangle|^2\delta(E-E_n+E_m). \end{aligned} \tag{A2}$$

where $E_m = 0$ and $E_n = 0$ for the creation and annihilation, respectively. In an equilibrium state at T, the probability is

$$W_m = Z^{-1}\exp\left(-\frac{E_m}{k_{\rm B}T}\right), \tag{A3}$$

where Z is the partition function: $Z = \sum_m \exp(-\frac{E_m}{k_{\rm B}T})$. Using $E_{nm} = E_n - E_m$, energy loss for the $|m\rangle \rightarrow |n\rangle$ transition, we obtain

$$S(\mathbf{q},\ E) = \exp\left(\frac{E_{nm}}{k_{\rm B}T}\right)S(-\mathbf{q},\ -E). \tag{A4}$$

Using the time-reversal invariant relationship $S(\mathbf{q},\ -E) = S(-\mathbf{q},\ -E)$, we obtain the formula for the principle of detailed balancing:

$$\frac{I_{\rm gain}}{I_{\rm loss}} = \frac{I(\mathbf{q},\ -E)}{I(\mathbf{q},\ E)} = \frac{S(\mathbf{q},\ -E)}{S(\mathbf{q},\ E)} = \exp\left(-\frac{E_{nm}}{k_{\rm B}T}\right). \tag{A5}$$

Equation (A5) is a general formula describing the relationship of interaction between an incident electron and a many-body system. For single-electron-phonon two-body scattering, we can write $E_{nm} = E_{\rm ph}$ in Eq. (A5) and obtain Eq. (1). In practical measurements, I is the integrated value within the wave-vector-selected aperture. Equation (A5) is satisfied when the center of the wave-vector-selected aperture is located at any $\mathbf{q}_\perp$. Equation (A5) holds in the steady state, whereas nonequilibrium statistical mechanics is required for the nonsteady state.

Regarding W_m [Eq. (A3)], Fig. 8 shows plots of the rates of finding LA and TO + LO phonons ($W_{\rm LA}$ and $W_{\rm TO+LO}$), relative to the rate of finding TA phonon ($W_{\rm TA}$), using experimental phonon energies (i.e., 124.5, 151.8, and 68.9 meV in the LA, TO + LO, and TA modes, respectively) at 323 K in Fig. 4. The ratios $W_{\rm LA}/W_{\rm TA}$ and $W_{\rm TO+LO}/W_{\rm TA}$ at 323 K are 0.153 and 0.046, respectively.

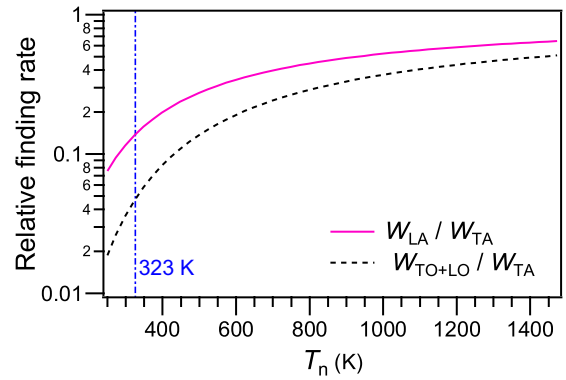

FIG. 8. Temperature dependence of the relative finding rates $W_{\rm LA}/W_{\rm TA}$ and $W_{\rm TO+LO}/W_{\rm TA}$ with experimental phonon energies [i.e., 124.5, 151.8, and 68.9 meV for longitudinal acoustic (LA), transverse optical (TO) + longitudinal optical (LO), and transverse acoustic (TA), respectively] in Fig. 4.

[1] D. G. Cahill, K. Goodson, and A. Majumdar, J. Heat Transfer **124**, 223 (2001).

[2] D. G. Cahill, W. K. Ford, K. E. Goodson, G. D. Mahan, A. Majumdar, H. J. Maris, R. Merlin, and S. R. Phillpot, J. Appl. Phys. **93**, 793 (2003).

[3] P. Verma, Chem. Rev. **117**, 6447 (2017).

[4] S. Kawata, T. Ichimura, A. Taguchi, and Y. Kumamoto, Chem. Rev. **117**, 4983 (2017).

[5] J. Langer, D. J. de Aberasturi, J. Aizpurua, R. A. Alvarez-Puebla, B. Auguié, J. J. Baumberg, G. C. Bazan, S. E. J. Bell, A. Boisen, A. G. Brolo *et al.*, ACS Nano **14**, 28 (2020).

[6] F. Niekiel, S. M. Kraschewski, J. Muller, B. Butz, and E. Spiecker, Ultramicroscpy **176**, 161 (2017).

[7] M. Mecklenburg, W. A. Hubbard, E. R. White, R. Dhall, S. B. Cronin, S. Aloni, and B. C. Regan, Science **347**, 629 (2015).

[8] L. He and R. Hull, Nanotechnology **23**, 205705 (2012).

[9] P. Jacobson and S. Stoupin, Diamond Relat. Mater. **97**, 107469 (2019).

[10] O. L. Krivanek, T. C. Lovejoy, N. Dellby, T. Aoki, R. W. Carpenter, P. Rez, E. Soignard, J. Zhu, P. E. Batson, M. J. Lagos *et al.*, Nature (London) **514**, 209 (2014).

[11] J. C. Idrobo, A. R. Lupini, T. Feng, R. R. Unocic, F. S. Walden, D. S. Gardiner, T. C. Lovejoy, N. Dellby, S. T. Pantelides, and O. L. Krivanek, Phys. Rev. Lett. **120**, 095901 (2018).

[12] M. J. Lagos and P. E. Batson, Nano Lett. **18**, 4556 (2018).

[13] D. Pines and P. Nozieres, *The Theory of Quantum Liquids* (Benjamin Inc., New York, 1966).

[14] C. Dwyer, T. Aoki, P. Rez, S. L. Y. Chang, T. C. Lovejoy, and O. L. Krivanek, Phys. Rev. Lett. **117**, 256101 (2016).

[15] J. Kikkawa, T. Taniguchi, and K. Kimoto, Phys. Rev. B **104**, L201402 (2021).

[16] K. Kimoto, in *Scanning Transmission Electron Microscopy of Nanomaterials: Basics of Imaging and Analysis*, edited by N. Tanaka (Imperial College Press, London, 2014).

[17] R. Senga, K. Suenaga, P. Barone, S. Morishita, F. Mauri, and T. Pichler, Nature (London) **573**, 247 (2019).

[18] F. S. Hage, R. J. Nicholls, J. R. Yates, D. G. McCulloch, T. C. Lovejoy, N. Dellby, O. L. Krivanek, K. Refson, and Q. M. Ramasse, Sci. Adv. **4**, eaar7495 (2018).

[19] R. Wang, H. Zobeiri, Y. Xie, X. Wang, X. Zhang, and Y. Yue, Adv. Sci. **7**, 2000097 (2020).

[20] F. Carbone, O.-H. Kwon, and A. H. Zewail, Science **325**, 181 (2009).

[21] Protochips, Inc., https://www.protochips.com/.

[22] P. Pavone, K. Karch, O. Schütt, D. Strauch, W. Windl, P. Giannozzi, and S. Baroni, Phys. Rev. B **48**, 3156 (1993).

[23] W. H. Richardson, J. Opt. Soc. Am. **62**, 55 (1972).

[24] L. B. Lucy, Astron. J. **79**, 745 (1974).

[25] K. Kimoto and K. Ishizuka, Ultramicroscopy **111**, 1111 (2011).

[26] R. F. Egerton, *Electron Energy-Loss Spectroscopy in the Electron Microscope* (Springer Science+Business Media, LLC, New York, 2011).

[27] A. Laubereau, D. von der Linde, and W. Kaiser, Phys. Rev. Lett. **27**, 802 (1971).

[28] E. S. Zouboulis and M. Grimsditch, Phys. Rev. B **43**, 12490 (1991).

[29] E. Haro-Poniatowski, J. L. Escamilla-Reyes, and K. H. Wanser, Phys. Rev. B **53**, 12121 (1996).

[30] G. Lang, K. Karch, M. Schmitt, P. Pavone, A. P. Mayer, R. K. Wehner, and D. Strauch, Phys. Rev. B **59**, 6182 (1999).

[31] A. C. Ferrari and J. Robertson, Phys. Rev. B **64**, 075414 (2001).

[32] S. M. Sze, *Physics of Semiconductor Devices* (John Wiley and Sons, New York, 1981).

[33] S. Bhattacharyya and S. R. P. Silva, Thin. Solid. Films **482**, 94 (2005).

[34] T. H. Borst and O. Weis, Phys. Stat. Sol (a) **154**, 423 (1996).

[35] A. J. Bullen, K. E. O'Hara, D. G. Cahill, O. Monteiro, and A. v. Keudell, J. Appl. Phys. **88**, 6317 (2000).

[36] Y. Yamamoto, T. Imai, K. Tanabe, T. Tsuno, Y. Kumazawa, and N. Fujimori, Diamond Relat. Mater. **6**, 1057 (1997).